Propellants, Explosives, Pyrotechnics

Propellants, Explosives, Pyrotechnics

RESEARCH ARTICLE OPEN ACCESS

AWSD Reactive Burn Model for the HMX-Based High Explosive LX-04

Galen T. Craven[1] | Joshua Finkelstein[1] | Kirill A. Velizhanin[1] | Stephen A. Andrews[2] | Jeffery A. Leiding[1] | Tariq D. Aslam[1] | Matthew A. Price[2] | Christopher Ticknor[2]

[1]Theoretical Division, Los Alamos National Laboratory, Los Alamos, New Mexico, USA | [2]X Computational Physics Division, Los Alamos National Laboratory, Los Alamos, New Mexico, USA

Correspondence: Galen T. Craven (gcraven@lanl.gov)

Received: 13 March 2026 | **Revised:** 8 May 2026 | **Accepted:** 23 May 2026

Keywords: high explosive | HMX | LX-04

ABSTRACT

An Arrhenius–Wescott–Stewart–Davis (AWSD) reactive burn model is applied to describe shock initiation and detonation properties of the HMX-based high explosive LX-04. The parameters in the model are calibrated to data from multiple sources. The thermodynamic equations of state used in the model are calibrated to a combination of thermochemical calculations for HMX and LX-04 as well as experimentally-measured cylinder expansion results for LX-04. The kinetic parameters are calibrated to velocity data from gas gun experiments performed using EDC-32—a high explosive with the same chemical composition as LX-04 but different structural properties, and scaled rate stick data for PBX 9012. The AWSD model is shown to accurately describe the shock initiation and propagation of LX-04. Very good agreement is observed between the available experimental data and the AWSD model output. The presented results constitute an accurate LX-04 reactive burn model for use in engineering-scale models and simulations.

1 | Introduction

LX-04 is an HMX-based high explosive (HE) consisting of 85% HMX and 15% Viton binder by weight [1, 2]. Viton—an inert binder—is a fluoropolymer that is added to HMX via plastic bonding techniques to increase safety, stability, and reliability of the resulting polymer-bonded explosive (PBX). The chemical composition of LX-04 is the same as EDC-32 [3] however the two HEs have different distributions of HMX particle sizes. Specifically, in LX-04 about 4% of the HMX particles by weight have sizes between 150 and 300 μm while in EDC-32 only a small percentage of large particles exist and ~99% of the particles by weight have a size less than 125 μm [3–5]. The chemical composition of LX-04 is similar to LX-07 and PBX 9012 which are both approximately 90% HMX and 10% Viton binder by weight [6–8]. Another explosive that uses the HMX-Viton combination is LX-10 which is 95% HMX and 5% Viton binder by weight [6, 9, 10]. Indeed there are a range of HEs that use the same energetic material (HMX) and binder (Viton) as LX-04, making it is possible to directly compare how varying binder percentage affects HE performance. LX-04 is an important HE primarily because of its potential application in engineering-scale systems [11] as well as its usefulness in understanding how damage can affect HE performance [2]. Developing theoretical tools that accurately describe the detonation and reactive burn of LX-04 is therefore an important topic, with potential applications and implications across several engineering subfields.

Reactive burn models are used to understand and predict the performance of HEs, specifically shock-initiation and detonation propagation properties [12–17]. In contrast to programmed burn models which use a simplified and pre-determined approach

to propagate the chemical reactions leading to detonation and shock propagation, reactive burn models include a reaction rate that depends upon the shock state. Here, we develop a reactive burn model for LX-04 using the Arrhenius–Wescott–Stewart–Davis (AWSD) model [17, 18]. The AWSD model is a reactive burn model that has successfully been applied to accurately model the behavior of a number of different HEs including LX-14 [19], PBX 9404 [20], PBX 9501 [21], PBX 9701 [18], and other HMX-based and TATB-based HEs [22–24]. These AWSD models have been shown to generally, and very accurately, capture the reactive burn of an HE after performing a calibration of the model parameters to different experimental sources such as velocity data from gas gun experiments with embedded electromagnetic velocity gauge packages, cylinder expansion (CYLEX) results, and diameter effect (rate stick) experiments.

The AWSD model [17] merges a Davis reactants equation of state (EOS) and a Davis products EOS [25–27] with an Arrhenius rate law [28–30] to describe the burn of the HE. The AWSD model can give very accurate results when compared to experiment and often outperforms other reactive flow models (see, for example, the results in Refs. [31] and [19]). One of the primary limitations of the AWSD model however, is that the functional forms for the chemical reaction rates are based on Arrhenius assumptions, meaning it is assumed that the HE is in thermodynamic equilibrium at the shock temperature and the energy in the system is Boltzmann distributed. Without modifications, complex chemical kinetics phenomena such as nanoscale thermal gradients and nonequilibrium distributions cannot be accounted for using an Arrhenius rate law model [32–37]. Additionally, it has been generally observed that the AWSD model overestimates the shock arrival velocity by a small but non-negligible amount in comparison to experimental gas gun results and other reactive burn models such as the CREST model [38]. That said, after calibrating the model parameters to data, the AWSD model generally gives excellent results, and can be used to describe a number of detonation properties and explain experimental results. The AWSD model is part of a long line of theoretical and computational treatments of high explosive detonations [17, 39–43].

Other reactive flow models have also been previously developed for LX-04. In 2018, Tarver reported an ignition and growth (I&G) model for LX-04 [1] using recent and also older experimental studies. This model was able to quite accurately describe CYLEX experiments performed under a variety of different conditions and experimental set-ups. Other metrics however, such as the shock-to-detonation transition (SDT) and shock propagation velocity profiles were not examined, so the validity of that model on multiple detonation phenomena has not yet been assessed. Chidester et al. also developed an I&G model for LX-04 that showed good agreement between the experimental and calculated run distances to detonation using manganin pressure gauge data [2]. They used that model to assess how LX-04 gas gun shots, performed in a relatively low pressure regime, are affected by the damage to the HE. A CREST model was developed for EDC-32 [5] which is in good agreement with gas gun shots and diameter effect results based on scaled values from other HEs. These previously developed models provide useful points of comparison and contrast for new reactive burn models of LX-04.

Experimental data has been reported for LX-04 and its chemically-identical counterpart EDC-32 in several sources, and this data can be used to calibrate the parameters in the AWSD model. Burns et al. performed a series of gas gun shots using EDC-32 [3] which provided shock waveform profiles, shock arrival times, time-to-detonation results, and also Hugoniot data for the reactants state. Additionally, CYLEX data is available for LX-04 in the open literature [1] and data on the Chapman–Jouguet (CJ) state of LX-04 is available from both Dobratz [44] and Wilkins [45].

In this article, we present results of an AWSD reactive burn calibration for LX-04. The model is calibrated to experimental data from the multiple sources described previously and is supplemented with thermochemical calculations performed using the `MAGPIE` code [46]. The AWSD model is shown to accurately describe shock initiation and subsequent shock propagation of LX-04 and overall, excellent agreement is observed between the available experimental data and our model.

2 | AWSD Model Calibration

2.1 | Reactants EOS

The AWSD model uses a Davis reactants EOS, which is an EOS that is commonly applied to describe the thermodynamic behavior of HEs. A full description of the analytical form for the Davis reactants EOS can be found in the Appendix and in Refs. [17] and [18]. The Davis reactants EOS is a Mie–Grüneisen EOS with nine parameters: A, B, C, $C_v^{(0)}$, Γ_0, Z, α_{st}, ρ_0, T_0. The nominal density of LX-04 is taken to be $\rho_0 = 1.86$ g/cm^3 [47, 48] and the nominal temperature is set to $T_0 = 297$ K. Values for the other parameters can be obtained by calibrating the EOS model to experimental data, thermochemical calculations, simulation data, or a combination of these sources.

The parameter A is the ambient sound speed of the material and can be interpreted as the intercept value of the shock velocity (U_S)- particle velocity (U_P) Hugoniot curve. After using an initial guess for this value of $A = 1.99$ km/s which is the PBX 9012 value from Burns and Chiquete in Ref. [7], we hand-tuned this parameter slightly to a value of $A = 2.00$ km/s in order to better match the shock arrival times in gas gun experiments from Burns et al. [3] discussed later in this work. The value of the Grüneisen gamma parameter Γ_0 was estimated using the method outlined by Burns and Chiquete in Ref. [7]. We tuned the parameters in this method starting with values for PBX 9012 (derived from LX-07 physical properties) as the starting point and adjusting for LX-04. The parameter Z is kept as 0 for thermodynamic consistency when $\rho = \rho_0$.

After setting the parameters ρ_0, T_0, A, Γ_0, and Z, the other parameters in the model ($B, C, C_v^{(0)}$, and α_{st}) were then calibrated by fitting the EOS to EDC-32 reactants Hugoniot data from Burns et al. [3], HMX Hugniot data from Marsh [49], and the HMX heat capacity model developed by Cawkwell [50]. The optimization was performed using Nelder–Mead optimization starting from the PBX 9501 parameter values as the initial guess [21], as is common with HMX-based HEs [19, 20]. Equal weighting was given to each of these data sources in the overall L_1 error

TABLE 1 | Reactants EOS parameters for LX-04.

Parameter	Value	Unit
A	2.0	kms^{-1}
B	3.97	
C	0.1214	
$C_v^{(0)}$	0.001003	$\text{kJg}^{-1}\,\text{K}^{-1}$
Γ_0	0.688	
Z	0	
α_{st}	0.4527	
ρ_0	1.86	gcm^{-3}
T_0	297.0	K

function used in the calibration. The parameter B determines the slope of the Hugoniot in the U_S-U_P plane at small U_P and the parameter C is related to the curvature of the Hugoniot. After calibration, we obtained values of $B = 3.97$ and $C = 0.1214$. The parameters $C_v^{(0)}$ and α_{st} appear in the Davis EOS heat capacity model and the calibration procedure resulted in values of $C_v^{(0)} = 0.001003\ \text{kJg}^{-1}\,\text{K}^{-1}$ and $\alpha_{st} = 0.4527$. A full listing of the calibrated Davis reactants EOS parameters for LX-04 is given in Table 1.

The results from the calibrated LX-04 reactants EOS are shown in Figure 1. The Hugoniot curve in the U_S-U_P plane is shown in Figure 1a, where U_S is the shock velocity and U_P is the particle velocity. The red circles denote experimental data for EDC-32 [3] and the black triangles are data for HMX single crystal data [49]. The orange dashed line depicts the HMX results computed using the `MAGPIE` code, and is included as reference [46]. At lower U_P values, the LX-04 Hugniot curve is highly nonlinear tending to the assigned ambient sound speed as $U_P \to 0$. However, comparing to the dashed black curve, which is the linear EOS given by Marsh, the Davis EOS and the linear EOS are in good general agreement at small U_P values. The green circular markers show Hugoniot data from Marsh for LX-04. Although this data was not used in the calibration, it is in excellent agreement with the calibrated Davis EOS. The LX-04 Hugoniot is less stiff than pure HMX, as expected, and this can be observed because the LX-04 curve always falls below the HMX curve. This is similar behavior to what is observed in other HMX-based polymer-bonded explosives. Figure 1b shows the Hugoniot curve in the P-V plane, where P is pressure and V is specific volume. The calculated EOS is in good agreement with the experimental data and appears to fit the data well across the full experimental data set. The green circular markers show Hugoniot data from Marsh for LX-04 that was not used in the model calibration, and this data exhibits excellent agreement with the calibrated Davis EOS.

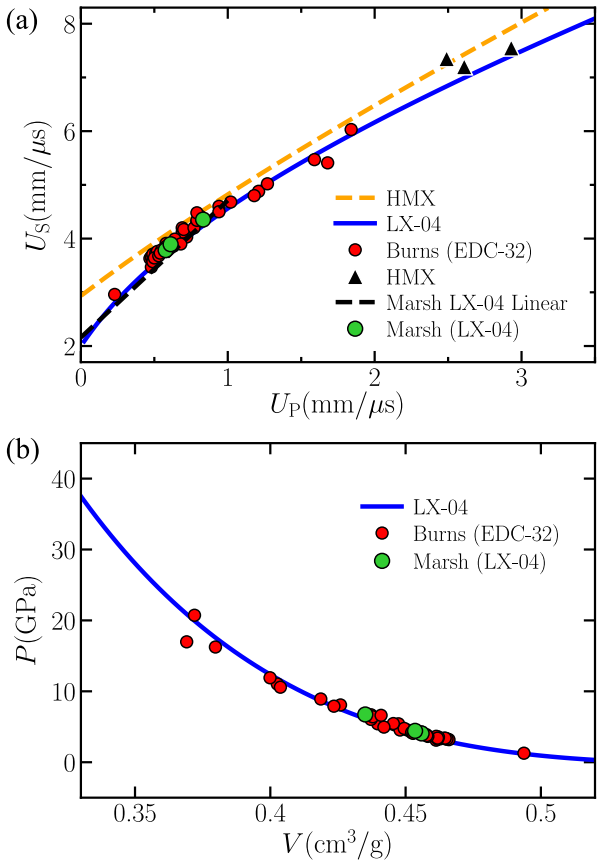

FIGURE 1 | Hugoniot curves for LX-04 reactants EOS calibrations in the (a) U_S-U_P and (b) P-V planes. The blue curves are the Davis EOS calibration for LX-04 performed in this work. The dashed orange curve in (a) is the result for HMX. The red circular markers correspond to experimental data for EDC-32 [3].The green circular markers are LX-04 Hugoniot data from Ref. [49]. The black triangular markers in (a) correspond to HMX single crystal data from Ref. [49]. The dashed black line in (a) is the linear EOS taken from Ref. [49].

2.2 | Products EOS

The Davis products EOS has seven parameters: a, b, k, n, p_c, v_c, C_{vp}, which can be calibrated by fitting the EOS model to available data sources. The stored chemical potential energy of the material E_{det} is derived from the products EOS after setting the other parameter values. A full description of the Davis products EOS can be found in the Appendix. Here, we used the CYLEX data for experiment K957 from Ref. [1] to calibrate the products EOS parameters. This experiment consisted of a 25.43 mm diameter LX-04 charge in a 2.58 mm thick copper tube. The wall velocities were measured using photon doppler velocimetry (PDV) probes. The Davis products parameters were optimized directly to the experimental data by minimizing the error between simulation and experiment wall velocities with a Nelder–Mead simplex algorithm. Simulations were conducted using FLAG, a multi-material, multi-physics hydrocode [51] with two-dimensional axial symmetry and initial zone size of 40 μm. The copper tube was modeled using a tabular SESAME EOS and the Preston–Tonks–Wallace (PTW) strength model [52]. While spall has been included in CYLEX simulations in previous EOS calibrations for some other HEs, we found that for LX-04 the effect of spall was minimal so it was neglected. The AWSD reactive burn region was initiated by a short 12.7 mm long section of programmed burn LX-04. Wall velocities obtained from the simulations are compared with PDV probe data from CYLEX experiments in Fig. 2.

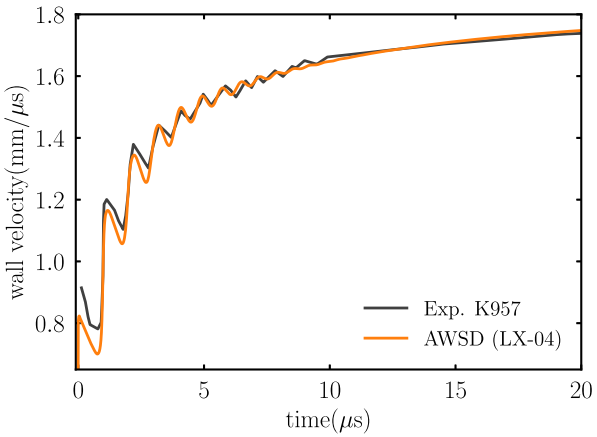

FIGURE 2 | Wall velocities from CYLEX simulations with the LX-04 AWSD calibration compared to experimental PDV data [1].

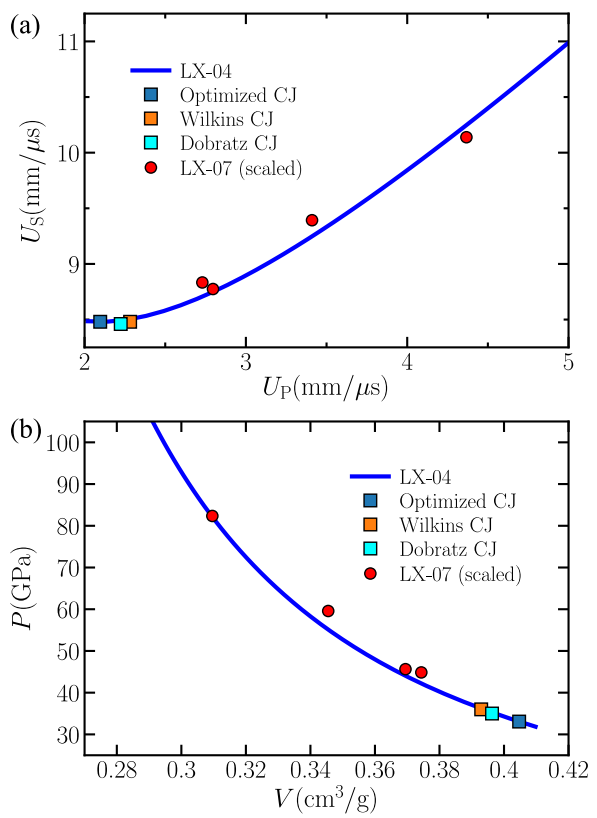

FIGURE 3 | Hugoniot curves for LX-04 products EOS calibrations in the (a) U_S-U_P and (b) P-V planes. The red circular markers correspond to experimental data for LX-07 [53] that is scaled by the ratio of the LX-04 and LX-07 detonation velocities. In each panel, the blue square marker is the CJ state calculated in this work, the cyan square marker is the CJ state reported by Dobratz [44], and the orange square marker is the CJ state reported by Wilkins [45].

The calibrated LX-04 products EOS Hugoniot curves are shown in Figure 3. Figure 3a shows the products Hugoniot curve in the U_S-U_P plane. The LX-04 CJ state given by Dobratz [44] is shown as a square cyan marker, the CJ state given by Wilkins [45] is shown as a square orange marker, and the corresponding state calculated using the calibrated/optimized Davis EOS is shown as a square dark blue marker. The CJ velocity from Dobratz is $D_{CJ}^{Dobratz}$ = 8.46 km/s, the value from Wilkins is $D_{CJ}^{Wilkins}$ = 8.48 km/s, and the optimized value is D_{CJ} = 8.48 km/s [11, 44, 45]. The red circular markers depict overdriven LX-07 datapoints [53] in which the U_S values have been scaled by a factor $D_{CJ}^{LX\text{-}04}/D_{CJ}^{LX\text{-}07}$, using a procedure similar to what is outlined by Anderson et al. [8]. The scaled LX-07 data is in good agreement with the calibrated Davis products EOS for LX-04. Figure 3b shows the products Hugoniot curves in the P-V plane. The value for the pressure at the CJ state given by Dobratz is $P_{CJ}^{Dobratz}$ = 35.0 GPa, the value from Wilkins is $P_{CJ}^{Wilkins}$ = 36.0 GPa, and the optimized value is P_{CJ} = 33.1 GPa. The scaled LX-07 data transformed into the P-V plane using standard Hugoniot relations is in good qualitative agreement with the calibrated Davis products EOS for LX-04.

TABLE 2 | Products EOS parameters for LX-04.

Parameter	Value	Unit
a	0.7562	
b	0.5881	
k	1.432	
n	1.575	
p_c	4.302	GPa
v_c	0.7754	$cm^3\ g^{-1}$
C_{vp}	0.001175	$kJg^{-1}\ K^{-1}$
E_{det}	5.355	kJg^{-1}

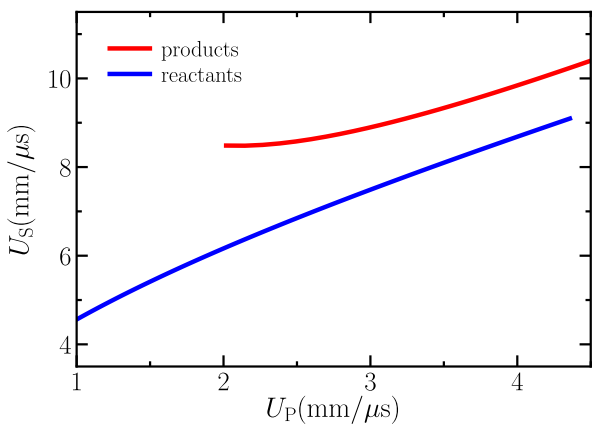

FIGURE 4 | Comparison between U_S-U_P curves for the LX-04 products EOS (red) and reactants EOS (blue).

A complete list of calibrated parameter values for the LX-04 Davis products EOS is given in Table 2.

Figure 4 shows a comparison between the Hugoniots for the products EOS and reactants EOS in the U_S-U_P plane. The primary observation is that the two functions do not cross. This non-crossing behavior is generally preferred for use in hydrodynamics codes as the non-crossing criteria reflects the positive thermicity of HEs.

2.3 | Rate Law

The AWSD model is a reactive flow (or, burn) model, in which the thermodynamic state of the shock initiation/propagation processes are determined by solving chemical kinetics equations. This compares to programmed burn models which rely on a predetermined approach to propagate the chemical reactions that lead to detonation and shock propagation.

A reactive flow method that extended the WSD (Wescott–Scott–Davis) model [54] by using Arrhenius forms for the chemical reaction rates to describe the transition Reactants → Products was previously developed, and is called the Arrhenius–Wescott–Stewart–Davis model or more succinctly the AWSD model. In the AWSD model, the reaction progress is determined by the dynamical evolution of a collective variable λ. This reaction progress variable takes a value of $\lambda = 0$ when the system consists entirely of reactant and $\lambda = 1$ when the system consists completely of product. We can therefore interpret λ as the mass fraction of product. The AWSD reaction rate is then determined by λ, the shock temperature T_{shock}, the pressure p and is defined through the relation

$$\frac{D\lambda}{Dt} = R(T_{\text{shock}}, p, \lambda), \tag{1}$$

where $\frac{D\lambda}{Dt}$ is the material derivative and R is the rate expression. The specific functional form for the rate expression in the AWSD model is given by

$$R(T_{\text{shock}}, p, \lambda) = F_p(F_1 + F_2)F_\lambda \tag{2}$$

where

$$F_p = \begin{cases} \exp[-(p_s/p)^{n_p}], & p > p_\zeta, \\ 0, & \text{otherwise}, \end{cases} \tag{3}$$

$$F_1 = k_1 \exp[-T_1/T_{\text{shock}}](\lambda + a_1 F_p)(1-\lambda)^{b_1}, \tag{4}$$

$$F_2 = k_2 \exp[-T_2/T_{\text{shock}}](1-\lambda)^{b_2}, \tag{5}$$

and

$$F_\lambda = f_s + \frac{1}{2}(1-f_s)\left(1 - \tanh\left[\frac{\lambda - \lambda_c}{\delta_\lambda}\right]\right). \tag{6}$$

See Ref. [17] for the derivation of these functional forms and detailed descriptions of what each of these functions represents. The AWSD rate law has 16 free parameters: p_s, p_ζ, T_1, T_2, T_c, a_1, a_T, b_1, b_2, δ_λ, f_s, k_1, k_2, k_ζ, λ_c, n_p. The parameters T_c and a_T arise from the definition

$$T^*(T, \lambda) = T(1 - a_T \exp[T_c/T]\lambda), \tag{7}$$

which is equal to the shock temperature when no reaction has taken place, that is, when $\lambda = 0$. The values for T_c and a_T are determined by examining the temperature profile through the reaction zone for a variety of initial HE temperatures [23]. T^* is optimized to be at or below the shock temperature. The values for all the other parameters can be assigned by performing a calibration to available data for the specific material being modeled, using values from AWSD calibrations for other HEs, empirical arguments, and/or simulation results. In practice, the data used to perform this calibration typically comes from some combination of gas gun and rate stick experimental data, and previous experience developing other AWSD models.

TABLE 3 | Gas gun data sources used in this work from Ref. [3].

shot #	ρ_0(g/cc)	Impactor	P(GPa)	Shock Type
1S-1468	1.861	Sapphire	5.59	Sustained
1S-1469	1.860	Sapphire	3.34	Sustained
1S-1470	1.861	Sapphire	4.83	Sustained
1S-1471	1.860	Quartz	3.28	Sustained
2S-493	1.861	Kel-F81	6.14	Short/Thin
2S-494	1.861	Kel-F81 & Vistal	4.20/8.79	Double Shock

Burns et al. performed a series of embedded particle velocity gauge measurements of EDC-32 at different pressures using gas–gun plate-impact techniques. A list of the Burns et al. gas gun shots we use in this work, as well as the pressure for each of those shots, is given in Table 3. Anderson et al. have reported PBX 9012 rate stick data in Ref.[8]. We are not aware of any rate stick experiments for LX-04, so to fill this gap in data we use the PBX 9012 data scaled by a factor $D_{\text{CJ}}^{\text{LX-04}}/D_{\text{CJ}}^{\text{PBX 9012}}$. Note that the available PBX 9012 data only captures a regime covering a small detonation decrease relative to D_{CJ}. This will be discussed in more detail later.

Starting from the reactants and products EOS for LX-04 described in previous sections, we calibrated the rate law parameters p_s, T_1, a_1, b_1, k_1, k_2, n_p in the AWSD model by fitting Eq. (1) to four of the Burns et al. gas gun shots (1S-1468, 1S-1469, 1S-1471, 2S-493). The first three shots are sustained shock experiments while shot 2S-493 is a thin pulse shot. The other parameters in the model were set using values from other AWSD calibrations and empirical knowledge/experience from reactive burn models of other HMX-based HEs. The data from shots 1S-1470 was withheld from the calibration so that we could then validate the AWSD model on data that was not used to assign parameters. This is a general test of the transferability of the calibrated model to different shock states. In this case because the pressure of shot 1S-1470 lies between two other shots, this is a test of model interpolation, rather than extrapolation from the calibration data. After completing the calibration, we also validated the model on shot 2S-494, which was a double shock experiment.

We employ an iterative technique that calibrates different subsets of parameters using different experimental data sources. Specifically, we calibrated the model parameters that determine the low-temperature and high-temperature AWSD rates to gas gun data and rate stick data, respectively, by iterating between the two regimes until an acceptable level of convergence was reached in the model. Convergence is defined here as a state in the optimization in which the parameters were essentially constant (up to some numerical threshold) as more iterations were performed and the overall model output was not changing significantly.

The first step in the calibration process was to assign values for the parameters using previous calibration data. These values were kept constant in the calibration procedure that follows. Next, a

TABLE 4 | AWSD parameters for LX-04.

Parameter	Value	Unit
p_s	42.15	GPa
p_ζ	0.6	GPa
T_1	1039	K
T_2	6000	K
T_c	575	K
a_1	0.1873	
a_T	0.4049	
b_1	2.427	
b_2	0.6	
δ_λ	0.01	
f_s	0.01	
k_1	593	μ^{-1}s
k_2	7461.35	μ^{-1}s
k_ζ	20	μ^{-1}s
λ_c	0.98	
n_p	0.446	

Nelder–Mead simplex optimization algorithm was used to obtain an initial set of optimized parameter values for p_s, T_1, a_1, b_1, k_1, n_p. The target goal in this step was to minimize the error between the AWSD model and the experimental data from shots 1S-1468, 1S-1469, 1S-1471, 2S-493. The initial guesses for the parameter values used in the optimization were taken to be the PBX 9501 values from Ref. [21]. The optimization procedure was performed for 400 iterations. The L^1 error for each gauge and each shot was calculated and then these error values were combined into a single total error metric. The goal of the Nelder–Mead procedure was to minimize this total error.

In the next step, rate-stick experiments were simulated using a shock-fitting code [55, 56] to calibrate the parameter k_2. The calibration in this step was performed using a variational Bayesian method [57].

In the final step of the calibration, the Nelder–Mead simplex optimization procedure was again performed to obtain the final parameter values for p_s, T_1, a_1, b_1, k_1, and n_p with the target goal of matching the gas gun experimental data. The mesh size used in the simulations was 20 μm, and the simulations were performed using the multimaterial multiphysics hydrocode `FLAG`. The gas-gun impactors were either Sapphire, Quartz, Vistal, or Kel-F81, depending on the shot. The impactor materials were modeled with a linear U_S-U_P EOS.

The final parameter values used in AWSD rate law are given in Table 4.

2.4 | Shock-to-Detonation Transition

Figure 5 presents a comparison between the SDT results predicted by the calibrated LX-04 AWSD model and the experimental data from each of the four shots used in the calibration. In each subplot of Figure 5, the experimental data is represented by the noisy dashed curves while the solid curves depict the output of the AWSD model. Overall very good agreement of AWSD model with the experimental results is observed for each shot. Equation of state values for the impactor materials can be taken from Table I in Ref. [3].

Shown in Figure 5a are the results for shot 1S-1468 which had an initial pressure of 5.59 GPa. For the early gauges, the wavefront shapes, shock arrival times, and maximum velocity magnitudes predicted by the AWSD model are all in excellent agreement with the data for each gauge. For the later gauges the shock arrival times are overestimated by the model in comparison to the experiments. Overall, AWSD model output is in very good/excellent agreement with the experimental data for this shot.

The SDT results for shots 1S-1469 are shown in Figure 5b. This was a low pressure shot that did not reach detonation. The results of low-pressure shots are often difficult to capture using the AWSD model. For LX-04, the AWSD model fit to this low-pressure shot is good. The shock arrival times, waveform shapes, and maximum velocites are in very good agreement for all gauges. The particle velocity at the shock are generally slightly overestimated by the model.

Figure 5c shows the results for shot 1S-1471 and which was a shot performed using Quartz as the flyer material. The pressure of this shot was 3.28; GPa, so it is the lowest pressure shot we examined in this work (see Table 3). Note the longer run-to-detonation for this shot compared to the other shots in Fig. 5. Very good agreement is observed for the shock arrival times. The velocity waveform shapes also have good agreement, with gauge 2 (the red curve) being the gauge with the worst agreement between experiment and model output—the other gauges were generally well captured by the model though the maximum shock velocity is overestimated in the middle gauges. Overall, this shot is well-captured by the AWSD model and reflects the ability for the model to be transferable across different flyer materials.

The results for the two-stage shot 2S-493 are shown in Figure 5d. The the shock releases of the last two gauges were not well captured in the experiment so there are only eight gauges shown for this shot. The pressure of this shot was 6.14 GPa. In this relatively high-pressure regime, the AWSD model captures the behavior of the detonation of LX-04 well. The particle velocity at the shock predicted by the AWSD model are in good agreement with the experimental values. The waveform shapes are also in good overall agreement, however a problem with the AWSD model is that the maximum shock velocities are overestimated which generates a mismatch between the wavefront shapes for each gauge. The detonation time is well predicted by the AWSD model, as can be seen by the accurate prediction of the shock arrival times of each gauge.

The data from shot 1S-1470 was not used in the rate law calibration procedure, and can therefore be used as validation of the model performance on unseen data. A comparison between the calibrated model and the experimental results for this shot are overlayed in Figure 6. Excellent agreement is observed between the LX-04 AWSD model the experimental data. Interestingly,

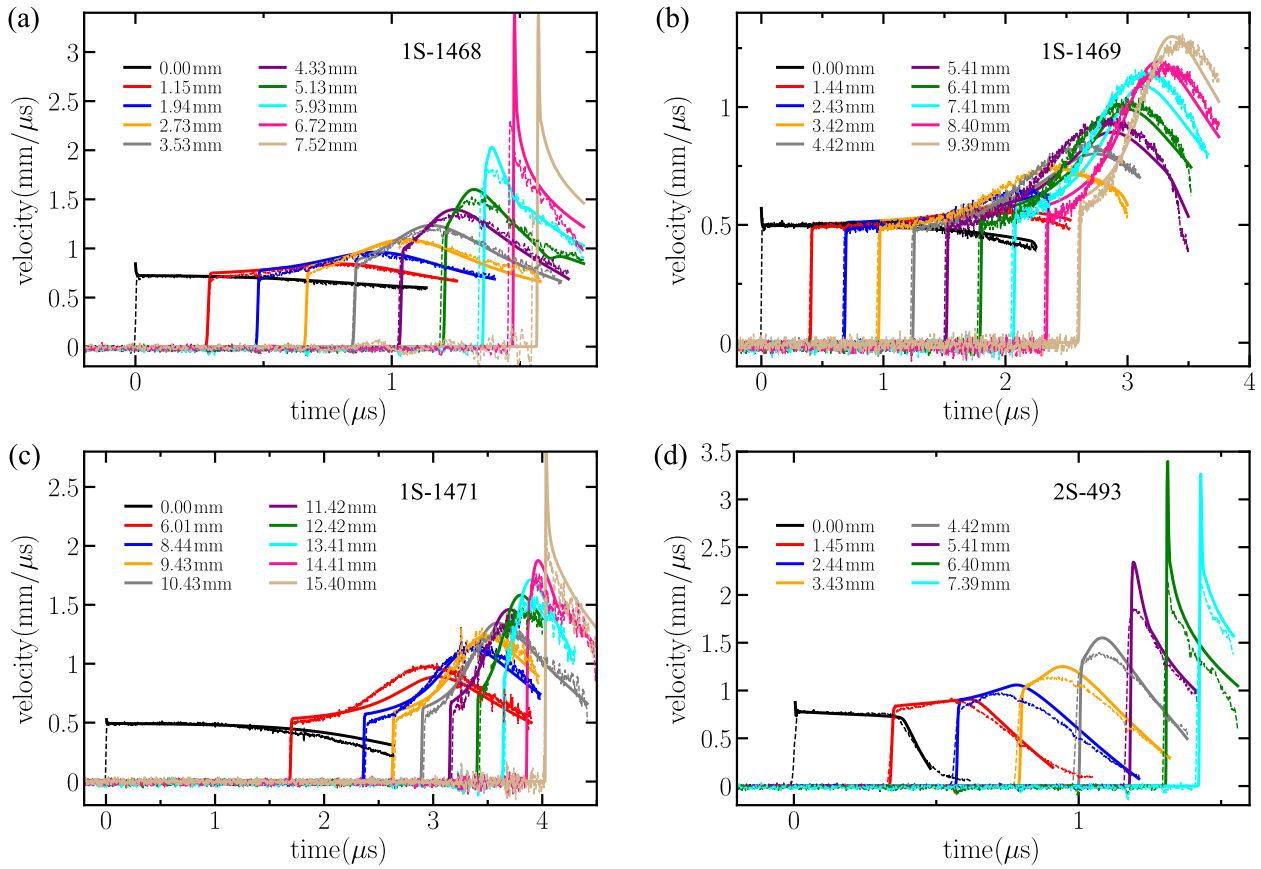

FIGURE 5 | Shock-to-detonation results for the LX-04 AWSD model developed here (solid lines) and experimental data from Ref. [3] from embedded electromagnetic gauge experiments (dashed lines) for shots (a) 1S-1468, (b) 1S-1469, (c) 1S-1471, and (d) 2S-493. The locations of the embedded gauges for each shot are shown in the corresponding legend. The gauge with value 0.00 mm represents the impact interface with the other gauges at the depths in the HE as indicated.

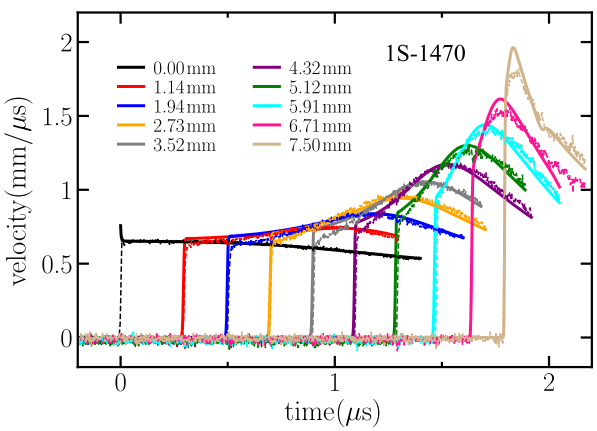

FIGURE 6 | Shock-to-detonation results for the LX-04 AWSD model (solid lines) and experimental data (dashed lines) for shot 1S-1470 [3]. This shot was not used in the calibration performed in this work. The locations of the embedded gauges are shown in the legend.

the model performance on this shot appears to be the best of any of the examined shots, even though it was not used in the calibration. This illustrates the predictive capability of the calibrated model on data that was not used to derive values for the model parameters. The shapes of the wavefronts for each gauge are well-captured by the model and are in excellent agreement with the experimental results. The shock arrival times are also in excellent agreement. As with all the other shots in this work, the particle velocity at the shock are slightly overestimated by the model in the early gauges.

The results for the two stage shot 2S-494—a double shock experiment—are shown in Figure 7. Note that this shot was also not used in the calibration so the presented results can be interpreted as validation/testing data. Overall good/acceptable agreement is observed between the AWSD model and the data. The arrival velocities for both shocks are well captured by the model. The arrival times for the first shock are well captured, while the arrival times for the second shock are generally late in the AWSD model. Overall the predicted waveform shapes are in very good agreement with the data. The differences between the arrival times (the jump off times) for the second shock can be attributed to the fact that we calibrate the EOS to data in a specific thermodynamic regime, and the double shock experiment pushes the system into thermodynamic states that are not sampled in the data used to calibrate the model.

2.5 | Diameter Effect

The final AWSD diameter effect results are shown in Figure 8. Figure 8a shows the AWSD results for LX-04. The red circular

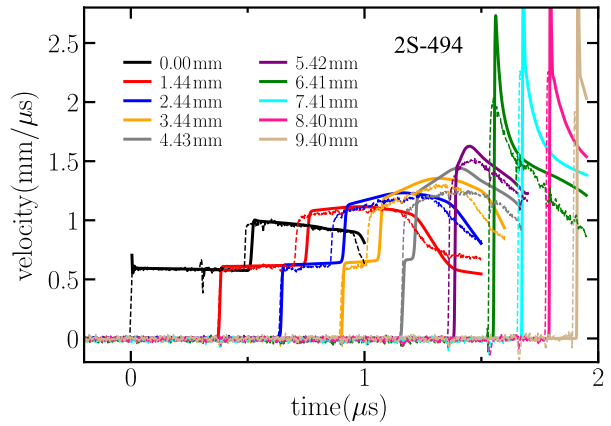

FIGURE 7 | Shock-to-detonation results for the LX-04 AWSD model (solid lines) and experimental data (dashed lines) for shot 2S-494 which was a double shock shot [3]. This shot was not used in the calibration performed in this work. The locations of the embedded gauges are shown in the legend.

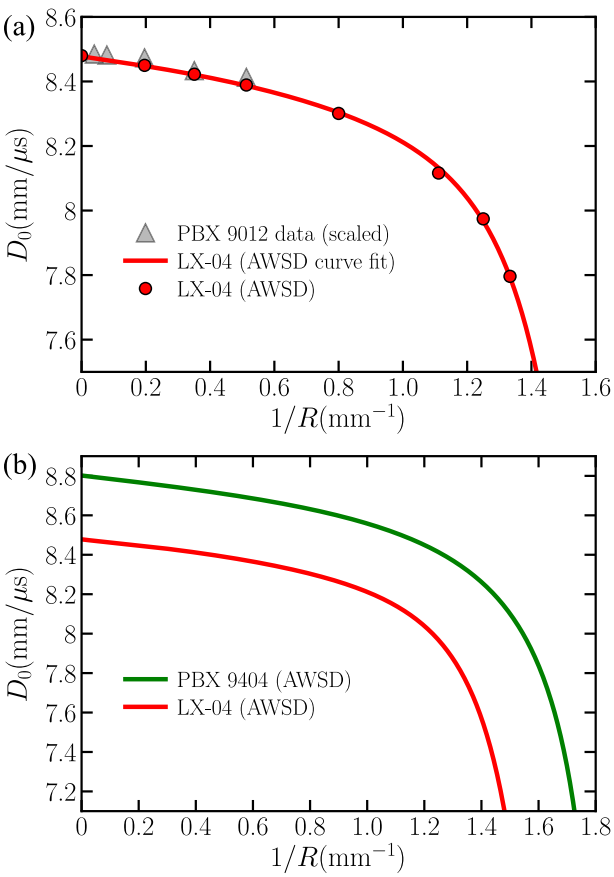

FIGURE 8 | Diameter effect results for LX-04. In panel (a), the gray triangular markers are data for PBX 9012 [8] scaled by a factor $D_{CJ}^{LX\text{-}04}/D_{CJ}^{PBX\ 9012}$, the red circular markers are the results of the AWSD simulation with the addition of a point with the detonation velocity for LX-04 of 8.48 mm/μs. The red solid curve is a fit to the simulation results. Panel (b) shows a comparison between the AWSD diameter effects results for PBX 9404 [20].

markers are the results of the AWSD simulation and the red curve is a fit to that simulation data shown to guide the eye. The gray triangular markers are data for PBX 9012 that has been scaled by a factor $D_{CJ}^{LX\text{-}04}/D_{CJ}^{PBX\ 9012}$ [8] where D_{CJ} denotes the CJ velocity. The hypothesized origin of this scaling as described by Anderson et al.,[8] is that changing the HMX content of an HE uniformly changes the energy available for propagation and does not affect the chemical kinetic pathways in the detonation. This in turn implies that the the energy release profile should be similar between the explosives LX-04 and PBX 9012. Both PBX 9012 and LX-04 use HMX and Viton as components, but in different mixture ratios (85% HMX, 15% Viton for LX-04 and 90.2% HMX, 9.8% Viton for PBX 9012). The AWSD result for LX-04 is in very good agreement with the available scaled data from PBX 9012. It should be noted that this agreement should be interpreted as reflecting both the expressivity of the AWSD model and potentially the true behavior of LX-04. Meaning if the scaled PBX 9012 data represents the true behavior of the LX-04, as the results by Anderson et al., suggest [8], then the model will quantitatively predict the behavior of LX-04. If this is not the case, then we anticipate that the AWSD model will only qualitatively reflect the diameter effects generated by LX-04. Validation of the predicted results would require LX-04 diameter effect results, which to our knowledge are not available in the open literature.

Figure 8b compares the AWSD diameter effect results for LX-04 and PBX 9404. The AWSD model predicts that LX-04 diameter effect behavior will fall below the 9404 results, as expected because of the high binder-to-HE ratio in LX-04 compared to PBX 9404. By comparing the PBX 9404 and LX-04 curves, it appears that the shape of the rate stick results can be approximately described by a systematic shift in magnitude given by the difference in the CJ velocities applied in the normal direction of each curve. For example, adding the factor $D_{CJ}^{PBX\ 9404} - D_{CJ}^{LX\text{-}04}$ to the normal direction along the LX-04 curve, would make the the PBX 9404 curve and the LX-04 curves be approximately overlapped. While we do not calibrate the LX-04 AWSD model to diameter effect data that is close to failure, the shown PBX 9404 model is calibrated to data in that regime. So, while there is uncertainty in the LX-04 AWSD model in the extrapolated regime close to failure, note that the general shape of the LX-04 diameter effect curve follows the shape of another HMX-based HE that is calibrated to data in that regime.

2.6 | Reactive Flow Model Comparison

Figure 9 shows a comparison between the CREST model for EDC-32 and the AWSD model for LX-04 using data for shot 1S-1468. Saying the results are for two different HEs is a semantic definition as we do not actually account for structural size distribution between the two HEs in the developed AWSD model. The CREST result is shown in Figure 9a and the AWSD result is shown in Figure 9b. We digitally extracted the CREST results from Ref. [5]. For the early gauges, the CREST model well-captures the shock arrival times, although not quite as accurately as the AWSD model. Comparing the waveform shapes for the CREST and AWSD model, it can be seen that the AWSD model more accurately reproduces those shapes, although the differences are subtle. For example, looking at gauges 1-5, the CREST model over-estimates the max shock velocity while the AWSD model gives

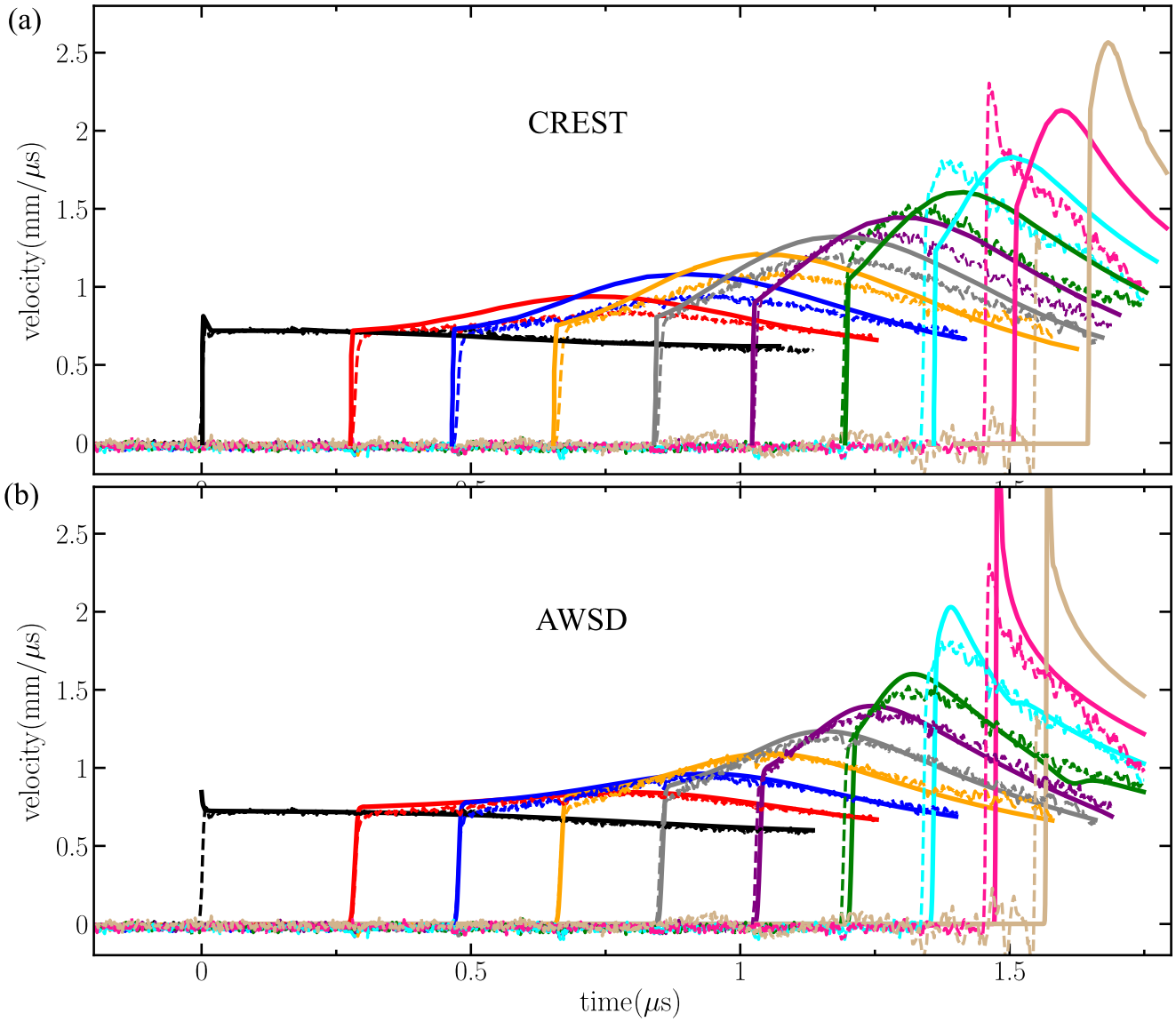

FIGURE 9 | Comparison of shock-to-detonation results for shot 1S-1468 using (a) the CREST model (b) the AWSD model. The experimental data is shown using dashed curves and the results for each respective model are shown using solid curves. Each different colored curve corresponds to a different gauge position, with the location of the gauges being shown in the legend of Figure 5a.

a result that is almost indistinguishable from the experimental result. The CREST model does not capture the correct time to detonation while the AWSD model provides a better estimate of the shock-to-detonation transition, although both overestimate this time compared to what is observed experimentally in shot 1S-1468. Overall, the AWSD performs better than the CREST model on this shot with respect to the overall error, but it should be noted the CREST model does capture the particle velocity at the shock more accurately than the AWSD model in the early gauges. The difference between the AWSD and experimental particle velocities could be due to a reduction in the particle velocity in the experimental data at the shock arrival due to gauge slip in the embedded gauges [58, 59].

It is important to note that the comparison between the CREST and AWSD models should not be interpreted as a direct comparison of overall model performance because the models were fit to different data sets. Specifically, different estimated size effect data was used in the two models, and so it is not overall surprising that the AWSD model performs well on the data we show here because it was directly calibrated to that data. It is also important to note estimated size effect data was used in both model calibrations, so the actual performance on modeling LX-04 and EDC-32 has uncertainty. Performing a comparison between the CREST and AWSD models on validation data in both interpolating and extrapolating data regimes would be a better test of model performance, and this is a direction for possible future work if/when new LX-04 data becomes available.

3 | Conclusions

The Arrhenius–Wescott–Stewart–Davis reactive burn model developed in this work provides an accurate description of the shock initiation and detonation behavior of the HMX-based high explosive LX-04. The parameters in the model were calibrated to

experimental data from gas gun, cylinder expansion, rate stick, and Chapman–Jouguet measurements as well as thermochemical calculations performed using the code MAGPIE. The resulting rate law parameters coupled with the calibrated equations of state for reactants and products quantitatively reproduce the experimentally observed shock-to-detonation transition characteristics across a wide range of impact pressures and over different flyer materials.

The calibrated AWSD model demonstrates good agreement with embedded gauge data from gas gun experiments and accurately captures many relevant phenomena in those experiments such as wavefront shapes, shock arrival times, maximum shock velocities, and time-to-detonation. Importantly, the model retains predictive capability on validation data that was not included in the fitting procedure, suggesting that the calibrated model will be transferable to experimental conditions and shock states that were not used in the calibration. We anticipate that the model will be suitable for use in large-scale hydrodynamic simulations requiring an accurate representation of LX-04 shock initiation and detonation kinetics. Furthermore, because LX-04 shares the same energetic material (HMX) and binder (Viton) with LX-07, PBX 9012, and LX-10, the presented parameter set potentially provides a basis for future comparative studies aimed at quantifying how binder content and particle-size distributions (for example, by comparing EDC-32 and LX-04) influence detonation performance. Work in this direction is currently underway.

The developed LX-04 model extends the recent set of AWSD calibrations for HMX-based HE compositions [19–22] and contributes to a broader effort of developing predictive reactive burn models for engineering-scale applications.

Acknowledgments

This work was supported by the U.S. Department of Energy through the Los Alamos National Laboratory.

Data Availability Statement

The authors have nothing to report.

References

1. C. M. Tarver. "Ignition and Growth Reactive Flow Modeling of Detonating LX-04 Using Recent and Older Experimental Data." in *AIP Conference Proceedings*, (AIP Publishing LLC, 1979, 2018): 100042.

2. S. K. Chidester, F. Garcia, K. S. Vandersall, and C. M. Tarver. "Shock Initiation Experiments Plus Ignition and Growth Modeling of Damaged LX-04 Charges." in *AIP Conference Proceedings*, 1195, (American Institute of Physics, 2009): 271–274.

3. M. J. Burns, R. L. Gustavsen, and B. D. Bartram, "One-Dimensional Plate Impact Experiments on the Cyclotetramethylene Tetranitramine (HMX) Based Explosive EDC32," *Journal of Applied Physics* 112, no. 6 (2012): 064910.

4. J. C. Millett, P. Taylor, A. Roberts, and G. Appleby-Thomas, "The Strength of two HMX Based Plastic Bonded Explosives During one Dimensional Shock Loading," *Journal of Dynamic Behavior of Materials* 3, no. 1 (2017): 100–109.

5. C. A. Handley and M. A. Christie. "Calibrating Reaction Rates for the CREST Model." in *19th Biennial American Physical Society Conference on Shock Compression of Condensed Matter 2015*, (2017): 030027.

6. L. Green, R. J. Wasley, and P. E. Kramer. "Shock Initiation of LX-07-2 and LX-10-0." Technical report, California Univ., Livermore. Lawrence Radiation Lab. (1970).

7. M. J. Burns and C. Chiquete, "Shock Initiation of the hmx-based Explosive pbx 9012: Experiments, Uncertainty Analysis, and Unreacted Equation-of-State," *Journal of Applied Physics* 127, no. 21 (2020): 215107.

8. E. K. Anderson, C. Chiquete, S. I. Jackson, R. I. Chicas, and M. Short, "The Comparative Effect of hmx Content on the Detonation Performance Characterization of pbx 9012 and pbx 9501 High Explosives," *Combustion and Flame* 230 (2021): 111415.

9. A. P. Wemhoff, W. M. Howard, A. K. Burnham, and A. L. Nichols III, "An LX-10 Kinetic Model Calibrated Using Simulations of Multiple Small-Scale Thermal Safety Tests," *Journal of Physical Chemistry A* 112, no. 38 (2008): 9005–9011.

10. J. W. Tringe, E. A. Glascoe, M. A. McClelland, D. Greenwood, R. D. Chambers, H. K. Springer, and H. W. Levie, "Pre-Ignition Confinement and Deflagration Violence in LX-10 and PBX 9501," *Journal of Applied Physics* 116 (2014): 054903.

11. M. K. Cichocki and D. Sokołowski, "Numerical Analysis of Shock Initiation on Highly Energetic Material LX-04," *Problems of Mechatronics, Armament, Aviation, Safety Engineering* 11 (2020): 57–66.

12. R. Menikoff and M. S. Shaw. "Reactive Burn Models and Ignition & Growth Concept." In *EPJ Web of Conferences*, 10 (2010): 00003.

13. D. E. Kittell, R. G. Schmitt, L. W. Tuttle, and E. N. Harstad. "Implementation of a CREST Multistate Reactive Burn Model in CTH for two Solid High Explosives." Technical report, Sandia National Lab.(SNL-NM), Albuquerque, NM (United States), (2018).

14. C. M. Tarver. "Ignition and Growth Reactive Flow Modeling of Recent HMX/TATB Detonation Experiments." in *AIP Conference Proceedings*, 1793 (2017): 030004.

15. Y. Yang, Z.-P. Duan, S.-R. Li, L.-S. Zhang, F.-L. Huang, Y. Han, and H. Huang, "A New Ignition-Growth Reaction Rate Model for Shock Initiation," *Defence Technology* 23 (2023): 126–136.

16. J. G. Christenson, M. P. Kroonblawd, S. Bastea, E. N. Weerakkody, K. S. Vandersall, and L. E. Fried, "Temperature-Based Reactive Flow Model for Triaminotrinitrobenzene (tatb) Plastic Bonded Explosives," *Journal of Applied Physics* 137 (2025): 115907.

17. T. D. Aslam, "Shock Temperature Dependent Rate Law for Plastic Bonded Explosives," *Journal of Applied Physics* 123, no. 14 (2018): 145901.

18. M. A. Price, J. A. Leiding, T. D. Aslam et al., "A Reactive Flow Model for the 3,3'-diamino-4,4'-azoxyfurazan Based Plastic Bonded Explosive (PBX 9701)," *Journal of Applied Physics* 130, no. 21 (2021): 215903.

19. G. T. Craven and C. Ticknor, "AWSD Reactive Burn Model for High Explosive LX-14," *Propellants Explosives Pyrotechnics* (2025): e12027.

20. G. T. Craven, M. A. Price, S. A. Andrews, K. A. Velizhanin, T. D. Aslam, J. A. Leiding, and C. Ticknor, "AWSD Reactive Flow Model for PBX 9404," *Journal of Applied Physics* 137, no. 13 (2025): 135903.

21. T. D. Aslam, M. A. Price, C. Ticknor, J. D. Coe, J. A. Leiding, and M. A. Zocher "AWSD Calibration for the HMX Based Explosive PBX 9501."*AIP Conference Proceedings* 2272, no. 1 (2020): 030001.

22. A. K. Henrick. "Davis EOS and AWSD Calibration for Octol." in *24th Biennial Conference of the APS Topical Group on Compression of Condensed Matter* LA-UR-25-29335, (2026).

23. T. D. Aslam. "A Recipe for Implementing the Arrhenius-Shock-Temperature State Sensitive WSD (AWSD) Model, With Parameters for PBX 9502." Technical Report LA-UR-17-24003, (Los Alamos National Laboratory, 2017).

24. M. A. Price, T. D. Aslam, and J. J. Quirk. "Validation of the AWSD Reactive Flow Model With PBX 9502 Experiments." in *16th Symposium (International) on Detonation*, (2018).

25. W. C. Davis. "Equation of State for Detonation Products." in *8th Symposium on Detonation*, (Albuquerque, NM, July 1985).

26. W. C. Davis. "Equation of State for Detonation Products." in *10th Detonation Symposium*, (Boston, MA, July 1993).

27. W. C. Davis. "Equation of State for Detonation Products." in *11th International Detonation Symposium*, (Snowmass, CO, July 1998).

28. R. Menikoff. "Arrhenius Rate: Constant Volume Burn." Technical Report LA-UR-17-31024, (Los Alamos National Laboratory, 2017).

29. R. C. Huber, J. Peterson, J. D. Coe et al., "Polysulfone Shock Compressed Above the Decomposition Threshold: Velocimetry and Modeling of Two-Wave Structures," *Journal of Applied Physics* 127, no. 10 (2020): 105902.

30. G. T. Craven. "Analytical Solutions of the Arrhenius-Semenov Problem for Constant Volume Burn." Technical Report LA-UR-21-31229, (Los Alamos National Laboratory, 2021).

31. M. A. Price. "A Study of Shock Initiation Experiments for the Explosive PBX 9502 Using Three Reactive Burn Models." in *AIP Conference Proceedings*, 2272, (AIP Publishing LLC, 2020): 070039.

32. M. Z. Bazant, "Theory of Chemical Kinetics and Charge Transfer Based on Nonequilibrium Thermodynamics," *Accounts of Chemical Research* 46, no. 5 (2013): 1144–1160.

33. G. T. Craven and R. Hernandez, "Lagrangian Descriptors of Thermalized Transition States on Time-Varying Energy Surfaces," *Physical Review Letters* 115 (2015): 148301.

34. G. T. Craven and A. Nitzan, "Electron Transfer Across a Thermal Gradient," *Proceedings of the National Academy of Sciences* 113 (2016): 9421–9429.

35. D. V. Matyushov, "Activated Kinetics in a Nonequilibrium Thermal Bath," *Proceedings of National Academy of Sciences* 113, (2016): 9401–9403.

36. I. Santamaría-Holek and A. Pérez-Madrid, "Eyring Equation and Fluctuation-Dissipation Far Away From Equilibrium," *Journal of Chemical Physics* 153, no. 24 (2020): 244116.

37. Z. A. Piskulich, O. O. Mesele, and W. H. Thompson, "Activation Energies and Beyond," *The Journal of Physical Chemistry A* 123, no. 33 (2019): 7185–7194.

38. C. A. Handley, "The CREST Reactive Burn Model," *Shock Compression of Condensed Matter* 955 (2007): 373–376.

39. C. M. Tarver, J. W. Forbes, and P. A. Urtiew, "Nonequilibrium Zeldovich-von Neumann-Doring Theory and Reactive Flow Modeling of Detonation," *Russian Journal of Physical Chemistry B* 1, no. 1 (2007): 39–45.

40. R. Menikoff, "On Beyond the Standard Model for High Explosives: Challenges & Obstacles to Surmount," *AIP Conference Proceedings* 1195, no. 1 (2009): 18–25.

41. R. Menikoff. "Detonation Wave Profile." Technical Report LA-UR-15-29498, (Los Alamos National Laboratory, 2015).

42. R. Menikoff "Introduction to High Explosives." Technical Report LA-UR-19-20814, (Los Alamos National Laboratory, 2019).

43. J. H. Peterson and J. D. Coe. "Beyond the Arrhenius Rate law in Simulating the Shock-Driven Decomposition of Polyimide." Technical Report LA-UR-20-20313, (Los Alamos National Laboratory, 2020).

44. B. M. Dobratz. *LLNL Explosives Handbook: Properties of Chemical Explosives and Explosives and Explosive Simulants*. (Lawrence Livermore National Lab.(LLNL), Livermore, CA, United States, 1981).

45. M. L. Wilkins, B. Squier, and B. Halperin, "Equation of State for Detonation Products of PBX 9404 and LX04-01." In *Symposium (International) on Combustion* 10 (1965): 769–778.

46. C. Ticknor, S. A. Andrews, and J. A. Leiding, "Magpie: A New Thermochemical Code," *in AIP Conference Proceedings* 2272, no. 1 (2020): 030033.

47. N. K. Bourne, "On the Critical Threshold for Detonation," *Combustion and Flame* 244 (2022): 112239.

48. B. W. White, J. E. Reaugh, N. Perez-Marty, and K. S. Vandersall, "A Low Velocity Impact Experiment for Obtaining Ignition Thresholds in Unconfined High Explosives." in *AIP Conference Proceedings*, 3066, (AIP Publishing LLC, 2024): 490025.

49. S. P. Marsh. *Lasl Shock Hugoniot Data*. (University of California Press, 1980).

50. M. J. Cawkwell, M. Zecevic, D. J. Luscher, and K. J. Ramos, "Complete Equations of State for Cyclotetramethylene Tetranitramine," *Propellants Explosives Pyrotechnics* 46, no. 5 (2021): 705–712.

51. D. E. Burton. "Multidimensional Discretization of Conservation Laws for Unstructured Polyhederal Grids." in *SAMGOP-94 2nd International Workshop on Analytical Methods and Process Optimization in Fluid and Gas Mechanics*, Holiday Base, Arzamas-16, Russia, 1994.

52. D. L. Preston, D. L. Tonks, and D. C. Wallace, "Model of Plastic Deformation for Extreme Loading Conditions," *Journal of Applied Physics* 93, no. 1 (2003): 211–220.

53. L. Green, E. Lee, A. Mitchell, and C. Tarver. "Supra-Compression of LX-07, LX-17, PBX-9404, and RX-26-AF and the Equations of State of the Detonation Products." Lawrence Livermore National Lab. CA, USA, 1985.

54. B. L. Wescott, D. S. Stewart, and W. C. Davis, "Equation of State and Reaction Rate for Condensed-Phase Explosives," *Journal of Applied Physics* 98 (2005): 053514.

55. C. M. Romick and T. D. Aslam, "High-Order Shock-Fitted Detonation Propagation in High Explosives," *Journal of Computational Physics* 332 (2017): 210–235.

56. C. M. Romick and T. D. Aslam, "An Extension of High-Order Shock-Fitted Detonation Propagation in Explosives," *Journal of Computational Physics* 395 (2019): 765–771.

57. S. A. Andrews and A. M. Fraser, "Estimating Physics Models and Quantifying Their Uncertainty Using Optimization With a Bayesian Objective Functional," *ASME Journal of Verification Validation and Uncertainty Quantification* 4, no. 1 (2019): 011002.

58. T. D. Aslam, D. M. Dattelbaum, J. A. Leiding, M. J. Cawkwell, C. Ticknor, S. A. Sheffield, and L. L. Gibson. "An Arrhenius-Wescott-Stewart-Davis (AWSD) Reactive Flow Model of Nitromethane." in *AIP Conference Proceedings*, volume 3066, page 480001. (AIP Publishing LLC, 2024).

59. J. B. Bdzil. "Fluid Mechanics of an Obliquely Mounted miv Gauge." Technical report, Los Alamos National Laboratory (LANL), Los Alamos, NM (United States), (2018).

Appendix A: Davis Reactants EOS

The Davis reactants EOS model is a Mie–Grüneisen EOS of the form

$$e_{\mathrm{R}}(p,\rho) = e_{\mathrm{R}}^{(s)}(\rho) + \frac{p - p_{\mathrm{R}}^{(s)}}{\rho\Gamma_{\mathrm{R}}(\rho)}, \tag{A1}$$

and

$$p_{\mathrm{R}}(e,\rho) = p_{\mathrm{R}}^{(s)}(\rho) + \rho\Gamma_{\mathrm{R}}(\rho)\Big(e - e_{\mathrm{R}}^{(s)}(\rho)\Big), \tag{A2}$$

where e is energy and p is pressure and the subscript "R" denotes the reactants state. The energy on the reference isentrope is

$$e_{\mathrm{R}}^{(s)}(\rho) = E_{\mathrm{det}} + \int_{\rho_0}^{\rho} \frac{p_{\mathrm{R}}^{(s)}}{\bar{\rho}^2}\, d\bar{\rho}, \tag{A3}$$

where E_{det} is the stored chemical potential energy of the material and the superscript "s" denotes that the quantity is calculated along the isentrope. The pressure on the isentrope is given by

$$p_{\mathrm{R}}^{(s)}(\rho) = \begin{cases} \hat{p}[\exp(4By) - 1], & \rho < \rho_0, \\ \hat{p}\left[\sum_{j=1}^{3} \frac{(4By)^j}{j!} + C\frac{(4By)^4}{4!} + \frac{y^2}{(1-y)^4}\right], & \rho \geq \rho_0, \end{cases} \tag{A4}$$

where $y = 1 - \rho_0/\rho$, and $\hat{p} = \rho_0 A^2/4B$. We take $\rho_0 = 1.86\ \mathrm{g/cm^3}$ for LX-04. Because we set $Z = 0$, the Grüneisen gamma function is given simply by

$$\Gamma_{\mathrm{R}}^{(s)}(\rho) = \Gamma_0, \tag{A5}$$

which can be compared to the piecewise form given in Ref. [17] which should be used when $Z \neq 0$. The temperature of the reactants is

$$T_{\mathrm{R}}(e,\rho) = T_{\mathrm{R}}^{(s)}(\rho)\left(\frac{1+\alpha_{st}}{C_v^{(0)} T_{\mathrm{R}}^{(s)}(\rho)}\left(e - e_{\mathrm{R}}^{(s)}(\rho)\right) + 1\right)^{\frac{1}{1+\alpha_{st}}}, \tag{A6}$$

where

$$T_{\mathrm{R}}^{(s)}(\rho) = T_0\left(\frac{\rho}{\rho_0}\right)^{\Gamma_0}, \tag{A7}$$

is the temperature along the isentrope and is given by a simplified form compared to the complete Davis EOS because $Z = 0$ in the LX-04 calibration. The specific heat in the Davis reactants EOS model is typically expressed using the functional form

$$C_v(T) = C_v^{(0)}\left(\frac{T}{T_0}\right)^{\alpha_{st}}, \tag{A8}$$

which is a function of temperature T and has three tunable parameters: T_0, $C_v^{(0)}$, and α_{st}. Here, the nominal temperature was set to $T_0 = 297$ K. The heat at the reference volume $C_v^{(0)}$ and the value of α_{st} are constants that are determined typically by fitting to HMX data, as specfiic heat values over a large temperature range are generally not known for PBX formulations.

Appendix B: Davis Products EOS

The Davis products EOS model is also a Mie–Grüneisen EOS of the form

$$e_{\mathrm{P}}(p,\rho) = e_{\mathrm{P}}^{(s)}(\rho) + \frac{p - p_{\mathrm{P}}^{(s)}}{\rho\Gamma_{\mathrm{P}}(\rho)}, \tag{B1}$$

and

$$p_{\mathrm{P}}(e,\rho) = p_{\mathrm{P}}^{(s)}(\rho) + \rho\Gamma_{\mathrm{P}}(\rho)\left(e - e_{\mathrm{P}}^{(s)}(\rho)\right), \tag{B2}$$

where e is energy and p is pressure as before with the subscript "P" denoting the products state. The pressure on principal CJ isentrope is

$$p_{\mathrm{P}}^{(s)}(\rho) = p_c \frac{\left[\frac{(\rho v_c)^{-n}}{2} + \frac{(\rho v_c)^n}{2}\right]^{a/n}}{(\rho v_c)^{-(k+a)}}\left(\frac{k-1+F(\rho)}{k-1+a}\right), \tag{B3}$$

where the density-dependent auxiliary function F is given by

$$F(\rho) = \frac{2a(\rho v_c)^n}{(\rho v_c)^{-n} + (\rho v_c)^n}. \tag{B4}$$

The Grüneisen gamma function is

$$\Gamma_{\mathrm{P}}(\rho) = k - 1 + (1-b)F(\rho). \tag{B5}$$

The energy on the isentrope is

$$e_{\mathrm{P}}^{(s)}(\rho) = e_c \frac{\left[\frac{(\rho v_c)^{-n}}{2} + \frac{(\rho v_c)^n}{2}\right]^{a/n}}{(\rho v_c)^{-(k-1+a)}}, \tag{B6}$$

with

$$e_c = \frac{p_c v_c}{k-1+a}. \tag{B7}$$

The products temperature is given by

$$T_{\mathrm{P}}(e,\rho) = T_{\mathrm{P}}^{(s)}(\rho) + \frac{e - e_{\mathrm{P}}^{(s)}(\rho)}{C_{vp}}, \tag{B8}$$

with the principal isentrope temperature given by

$$T_{\mathrm{P}}^{(s)}(\rho) = T_c \frac{\left[\frac{(\rho v_c)^{-n}}{2} + \frac{(\rho v_c)^n}{2}\right]^{(a/n)(1-b)}}{(\rho v_c)^{-(k-1+a(1-b))}}, \tag{B9}$$

where

$$T_c = \left(\frac{2^{-ab/n}}{k-1+a}\right)\left(\frac{p_c v_c}{C_{vp}}\right). \tag{B10}$$